

# Broadband magnetometry and temperature sensing with a light-trapping diamond waveguide

Hannah Clevenson<sup>1,2\*</sup>, Matthew E. Trusheim<sup>1</sup>, Carson Teale<sup>1,2</sup>, Tim Schröder<sup>1</sup>, Danielle Braje<sup>2\*</sup> and Dirk Englund<sup>1\*</sup>

**Solid-state quantum sensors are attracting wide interest because of their sensitivity at room temperature. In particular, the spin properties of individual nitrogen-vacancy (NV) colour centres in diamond<sup>1–3</sup> make them outstanding nanoscale sensors of magnetic fields<sup>4–9</sup>, electric fields<sup>10</sup> and temperature<sup>11–13</sup> under ambient conditions. Recent work on NV ensemble-based magnetometers<sup>14–16</sup>, inertial sensors<sup>17</sup>, and clocks<sup>18</sup> has employed unentangled colour centres to realize significant improvements in sensitivity<sup>15,19</sup>. However, to achieve this potential sensitivity enhancement in practice, new techniques are required to excite efficiently and to collect the optical signal from large NV ensembles. Here, we introduce a light-trapping diamond waveguide geometry with an excitation efficiency and signal collection that enables in excess of 5% conversion efficiency of pump photons into optically detected magnetic resonance<sup>20</sup> (ODMR) fluorescence—an improvement over previous single-pass geometries of more than three orders of magnitude. This marked enhancement of the ODMR signal enables precision broadband measurements of magnetic field and temperature in the low-frequency range, otherwise inaccessible by dynamical decoupling techniques.**

The NV's low absorption cross-section<sup>21</sup> has thus far prevented high conversion efficiency from excitation power to NV ODMR signal in bulk diamond samples using the typical single-pass excitation geometry illustrated in Fig. 1a. For NV densities around  $10^{15} \text{ cm}^{-3}$  (refs 5,22), for which the NV spacing in the diamond lattice is sufficiently sparse to maintain long spin coherence times<sup>6</sup>, up to metre-long path length would be necessary for significant excitation absorption (see Supplementary Information). Efficient collection has been demonstrated from NVs in single-pass excitation geometries<sup>14,15</sup>, but absorption is less than 1% for a typical 300- $\mu\text{m}$ -thick, electron-irradiated, type IIa diamond sample. Wide-field microscopy implemented with CCD (charge-coupled device) cameras can collect fluorescence from ensembles of up to  $10^3$  NV centres<sup>23</sup> in the focal volume of the objective, but suffers from low collection efficiency with most fluorescence emission trapped within the diamond owing to total internal reflection (TIR) at the diamond–air interface. External Fabry–Perot cavities could increase the optical depth<sup>16</sup> for green excitation, but would introduce bandwidth restrictions as well as the additional complexity of stabilized, narrow-linewidth excitation lasers.

We have designed and realized a new ensemble measurement scheme that overcomes these limitations. The light-trapping diamond waveguide (LTDW) consists of a rectangular diamond slab with a small angled facet at one corner for input coupling of the pump beam, as illustrated in Fig. 1b. The input facet has a

length  $a$  at an angle  $45^\circ$  relative to the square sample sides, allowing pump light to couple into the structure while being confined by TIR ( $\theta > \theta_c = 24.6^\circ$ ) on the other surfaces. Figure 1c shows an optical image of a pump beam coupled at an  $11.6^\circ$  angle into the LTDW ( $3 \text{ mm} \times 3 \text{ mm} \times 300 \mu\text{m}$ ). Red fluorescence is recorded with a colour CCD camera without spectral filtering. Figure 1d shows the corresponding numerical simulation of a Gaussian pump laser incident on an LTDW structure with the same dimensions. For clarity in visualizing light propagation, a non-optimal length pump path of only 6 cm is depicted. Simulations of path length versus incident angle in Fig. 2b indicate that the LTDW structure enables path lengths of over a metre. These numerical simulations (see Supplementary Information) account for beam divergence and for losses due to absorption. Scattering losses are neglected owing to the low surface roughness of the polished sample. In this ensemble sensor, the available pump power is limited, making efficient conversion of pump light into detected ODMR signal essential. We quantify this ‘pump-to-signal photon conversion’ as  $\eta_{\text{ODMR}} = \phi_{\text{det}}/\phi_{\text{p}}$ , where  $\phi_{\text{det}}(\phi_{\text{p}})$  is the photon flux detected (in the pump beam). Figure 2a depicts  $\phi_{\text{det}}$  versus  $\phi_{\text{p}}$  when the LTDW input facet is pumped with a 532 nm Gaussian beam ( $1/e^2$  diameter =  $300 \mu\text{m}$ ). Here,  $\phi_{\text{p}}$  is obtained from the power of the pump beam; the linear relationship indicates that the saturation is not reached even at relatively high pump power ( $\sim 2 \text{ W}$ ). The slope provides a conversion efficiency of  $\eta_{\text{ODMR}} = 2.6 \times 10^{-3}$ ; that is, approximately one red photon is detected for every 385 green pump photons. This efficiency is two or three orders of magnitude greater than when the diamond is pumped in a single-pass configuration along the long or short axis respectively. From our measurements, the fraction of pump photons converted into NV fluorescence (both collected and not collected) is  $\eta_f \sim 0.055$  (see Supplementary Information).

The LTDW's increased path length and the consequently large ODMR signal photon flux allows for high precision measurements of quantities that affect the NV's magnetic sub-levels. Figure 3a plots ODMR spectra obtained under continuous-wave microwave field excitation when a 3-mm-diameter loop of 200- $\mu\text{m}$ -diameter wire is placed 5 mm above the LTDW. An additional 2.5 mT static magnetic field applied along the [111] diamond crystal axis splits the degeneracy of the NV sub-level transitions  $m_s = 0 \rightarrow \pm 1$ . Of the four NV orientations supported in the diamond lattice, the  $\langle 111 \rangle$  sub-ensemble therefore shows the greatest Zeeman shift, as seen in the splitting between frequencies  $\omega_+$  and  $\omega_-$  (Fig. 3a), as its quantization axis is aligned with the magnetic field. The equal magnetic field projection onto each of the three remaining NV orientations results in their degenerate transition energies with three times the ODMR contrast compared with the  $\langle 111 \rangle$  sub-ensemble.

<sup>1</sup>Department of Electrical Engineering and Computer Science, Massachusetts Institute of Technology, Cambridge, Massachusetts 02139, USA.

<sup>2</sup>MIT Lincoln Laboratory, Lexington, Massachusetts 02420, USA. \*e-mail: hannahac@mit.edu; braje@ll.mit.edu; englund@mit.edu

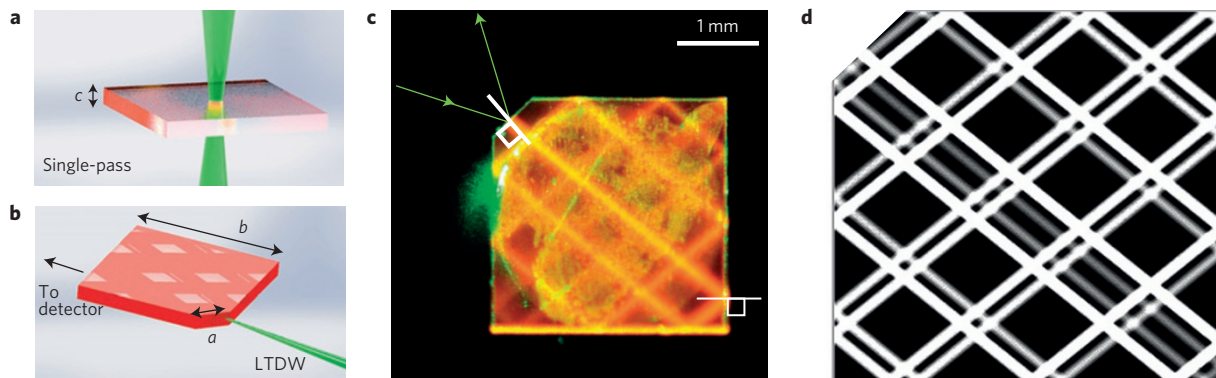


**Figure 1 | Light-trapping diamond waveguide.** **a**, Standard single-pass laser excitation exhibiting a short path length of interaction with NV centres as compared with the LTDW. **b**, For an equivalent excitation power, the LTDW increases the path length of the excitation beam by up to several orders of magnitude. **c**, The colour CCD image of the LTDW, excited by a green pump laser with a power of 70 mW, shows bright fluorescence without any spectral filtering. **d**, Simulation of the beam path in the LTDW with  $a = 500 \mu\text{m}$  input facet, 3 mm side length, 100- $\mu\text{m}$ -diameter Gaussian profile input incident at  $11.6^\circ$ , and an absorption constant of  $\alpha = 0.45 \text{ cm}^{-1}$ .

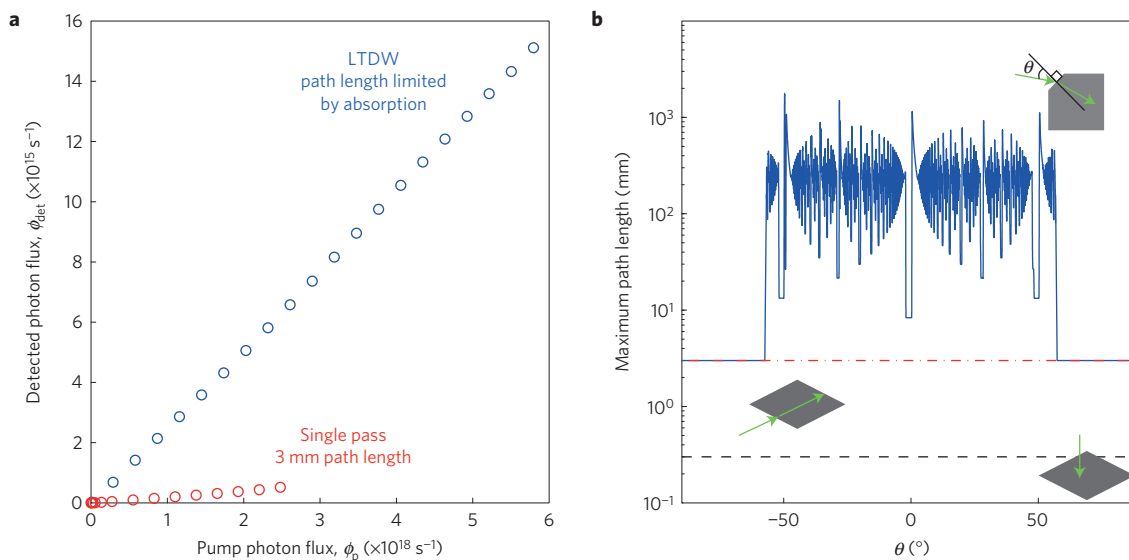


**Figure 2 | Optical properties of the LTDW.** **a**, Pump photon flux plotted against detected photon flux for the LTDW (blue) and for a single pass through the long side of the device (red). Error bars are contained within the data points. **b**, Maximum optical path length (unconstrained by absorption) plotted as a function of input angle into the LTDW structure with a  $150 \mu\text{m}$  input facet and standard beam divergence in blue. The excitation laser intersects the input facet  $50 \mu\text{m}$  from the centre, resulting in asymmetry in the plot. For comparison, the maximum optical path length achievable in a single-pass configuration through the top of the sample is also plotted in black, and through the side of the sample is plotted in red. In samples with sufficiently high NV density, the excitation beam would be absorbed before achieving the maximum path length allowed by the LTDW structure.

Hyperfine coupling of the NVs to the  $^{14}\text{N}$  nuclear spin splits each of the electronic sub-level transitions into Lorentzian triplets (Fig. 3c), which exhibit a full-width at half-maximum linewidth of 1.2 MHz spaced by  $\sim 2.1$  MHz.

We measure magnetic field and temperature shifts by monitoring the fluorescence of the LTDW at the  $m_s = 0 \rightarrow -1$  and the  $m_s = 0 \rightarrow +1$  transitions. The microwave excitation frequency,  $\omega_{\text{ODMR}}$ , is alternately tuned to the frequencies  $\omega_+$  and  $\omega_-$ , where the derivative of the ODMR signal with respect to frequency is greatest. Around these frequencies, we modulate  $\omega_{\text{ODMR}}$  at 1.5 kHz with a modulation depth of 1 MHz and use a lock-in amplifier to monitor the NV fluorescence. Figure 3b depicts the lock-in signal for a time constant of 10 ms.

From the ground-state, axial, hyperfine Hamiltonian (see Supplementary Information), it follows that the  $m_s = 0 \rightarrow \pm 1$  resonance frequencies are given by  $\omega_{\pm} \approx (D_{\text{gs}} + \beta_T \Delta T) \pm \gamma B_z$ , where  $D_{\text{gs}} \simeq 2.87 \text{ GHz}$  is the zero field splitting frequency due to

spin-spin interactions,  $\beta_T \approx -74 \text{ kHz K}^{-1}$  is the phenomenological temperature dependence of the NV centre's zero field splitting at room temperature<sup>24</sup> and the Zeeman shift in response to an axially applied magnetic field in the [111] crystal direction is  $\gamma = \mu_B g_s / h \approx 2\pi \times 28 \text{ GHz T}^{-1}$ , where  $\mu_B = (e\hbar)/(2m_e)$  is the Bohr magneton, and  $g_s \approx 2$  is the Landé  $g$ -factor. By sequentially monitoring both transitions,  $\omega_{\pm}$ , we obtain the mean value of  $\omega_{\pm}$ , which yields the temperature shift  $\Delta T$ , and the difference,  $\omega_+ - \omega_-$ , which provides the magnetic field shift<sup>25</sup>. Frequency analysis of the noise in the LTDW system (Fig. 4a) obtained at  $\omega_+$  only (no temperature compensation) indicates that at 1 Hz, the noise floor is less than  $0.5 \text{ nT Hz}^{-1/2}$ . Figure 4b plots independent measurements of temperature and magnetic field over a time period of 100 s. Each point represents an integration time of 10 ms and an equivalent bandwidth of 10 Hz, accounting for the lock-in amplifier roll-off. The measurement indicates a magnetic field measurement with standard deviation  $\sigma = 0.93 \text{ nT}$  across 10-s sampling intervals, which

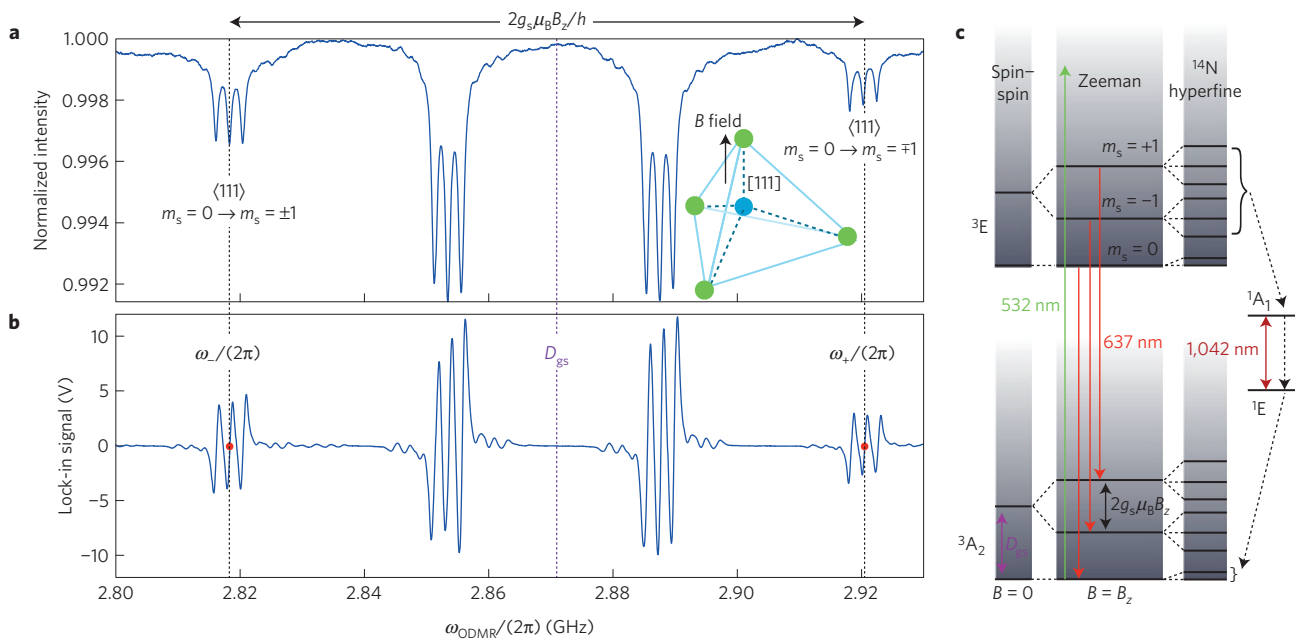


**Figure 3 | ODMR spectra and level structure.** **a**, Continuous-wave electron spin resonance with external magnetic field aligned along a single [111] crystal axis. The inset depicts the diamond lattice, where the blue circle represents the nitrogen atom and the green circles show the four possible orientations for the vacancy in the tetrahedral crystal lattice, constituting the four sub-ensembles of NVs. **b**, Lock-in output corresponding to signal in **a**. The scale factor ( $\text{V Hz}^{-1}$ ) is provided by a linear fit around each of the two red points. Temperature and magnetic field shifts are measured independently by tracking both  $m_s = \pm 1$ . **c**, Energy-level diagram of diamond NV centre showing radiative (solid lines) and non-radiative (dotted lines) transitions.

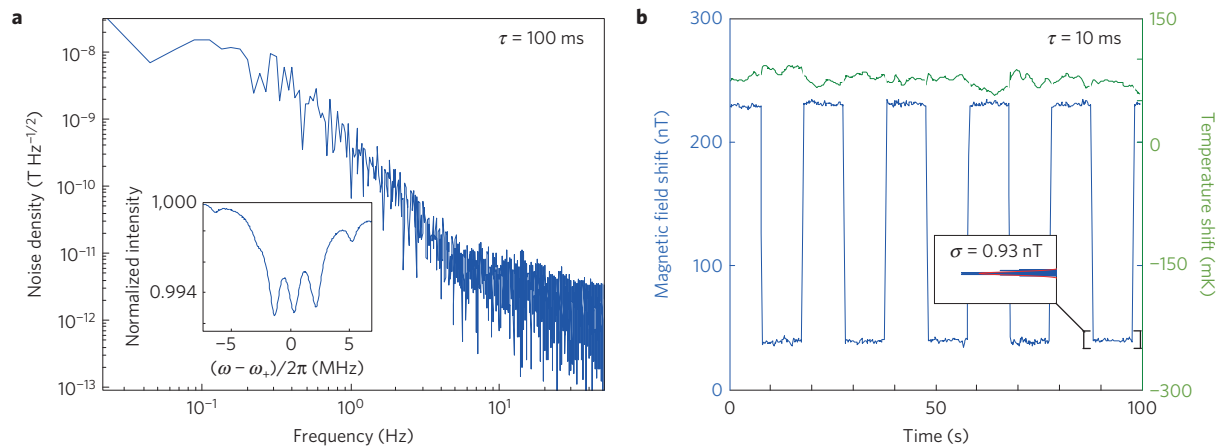


**Figure 4 | Sensitivity measurements.** **a**, Noise density of the in-phase lock-in amplifier signal at the  $\omega_+$  resonance (see inset) converted to units of magnetic field for a time constant of 100 ms; low frequency noise is attributed to thermal effects. **b**, Separation of magnetic field and temperature effects. Green and blue lines show the sum and difference of the intensity signals from lower and higher frequency resonances of the (111) orientation with a time constant of 10 ms, decoupling the temperature and magnetic field drifts over 100 s, respectively. A 20-s-period square wave of amplitude 190 nT is applied with external coils and is clearly visible in the blue trace. The noise on a single 10 s step (0.93 nT) extrapolates to  $\sim 290 \text{ pT Hz}^{-1/2}$  when accounting for the 10 Hz equivalent noise bandwidth of the lock-in amplifier. The green trace shows drift attributed to environmental effects; aliasing effects have been removed (less than 200 ms).

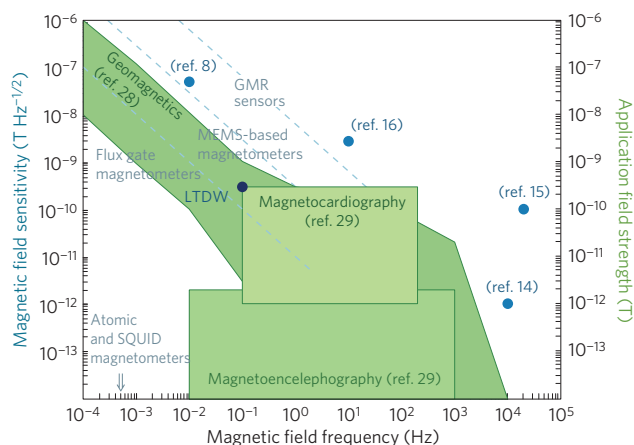
extrapolates to a sensitivity of  $290 \text{ pT Hz}^{-1/2}$  at 0.1 Hz (effectively DC). We separately resolve a gradual temperature shift during this measurement (green curve), within the expected range of temperature stabilization. Note that for this method of temperature and magnetic field shift separation, signal errors add in quadrature.

Figure 5 compares the LTDW magnetic field sensitivity (from Fig. 4b) with recently demonstrated NV magnetometers and other magnetometer platforms. Also indicated are the sensitivity requirements for three key magnetometer applications: magnetocardiography, magnetoencephalography, and the monitoring of geomagnetics. The unique position of the LTDW in the low-frequency limit makes it suited for a variety of magnetic field sensing

applications including medical monitoring, object detection, and the study of geomagnetics that occur in the  $10^{-4}$  to 10 Hz range. Although SQUID and atom-based magnetometry achieve better sensitivity at low frequencies, these technologies require cryogenics and vacuum systems that limit their practical use.

For high-frequency magnetic field measurements, Echo-type magnetometry could be employed with dynamic decoupling pulses to extend the NV electron spin coherence time<sup>5</sup>. In this regime, the sensitivity could approach the fundamental spin projection limit,

$$S = \delta B_{\text{min}} \sqrt{T} \simeq \frac{1}{\gamma} \frac{1}{\sqrt{N\tau}}$$



**Figure 5 | Comparison of the LTDW sensitivity with that of other magnetometry technologies.** Particularly with regard to target applications such as geomagnetics<sup>28</sup> shown in green (corresponding to the right axis), the LTDW (dark blue) achieves improved sensitivity with respect to other diamond-based sensors, shown in blue (corresponding to the left axis), in the important low-frequency band<sup>29</sup>. The LTDW's performance is competitive with other magnetometer platforms<sup>30</sup>, shown in light blue.

where  $\delta B_{\min}$  is the minimum detectable magnetic field,  $T$  is the measurement time,  $N = 10^{13}$  is the estimated total number of NV centres in our sample (see Supplementary Information), and  $\tau \sim 1$  ms is the electron spin dephasing time measured with dynamical decoupling in comparable samples and expected to be feasible for NV densities of the order of 1 ppm (ref. 5). Neglecting contrast and collection efficiency, these parameters predict a spin projection limit of up to  $S = 0.05$  fT Hz<sup>-1/2</sup>.

To improve on the LTDW design presented here, TIR geometries using quasi-chaotic excitation paths could also be used for NV excitation and may result in more uniform coverage of the bulk sample<sup>26</sup>. Although the facets of the LTDW are highly polished to a surface roughness of  $\sim 2$  nm root mean square (r.m.s.), scattering loss occurs at the edges and corners of the structure. Lower surface roughness would improve the TIR and reduce scattering losses. In addition, increasing ODMR contrast also would result in improved sensitivity.

In conclusion, we have introduced a dual magnetic field and temperature sensor based on an LTDW geometry that enables nearly complete green pump absorption and efficient spin-dependent fluorescence collection. With more than two orders of magnitude improvement in pump power conversion over previous single-pass schemes, the LTDW achieves high signal-to-noise sensing and sensitivity below nT Hz<sup>-1/2</sup> the low-frequency regime, which is not accessible by dynamical decoupling techniques. The low power requirement for the LTDW allows it to be implemented with a compact, inexpensive laser diode excitation source. We measure a magnetic field sensitivity of  $\sim 290$  pT Hz<sup>-1/2</sup> in the sub-100 Hz regime. In this low-frequency domain, such high-sensitivity magnetometers promise new applications for solid-state sensors in a range of fields including biomedical sensing and object detection. The light-trapping technique could be extended to transmission measurements and direct infrared absorption techniques<sup>16</sup>. The device is not limited to sensing; it could be used for any application requiring a long optical path length within the sample such as electromagnetically induced transparency-based experiments or optical quantum memories<sup>27</sup>. The LTDW provides a compact, portable precision sensor platform for measuring magnetic fields, temperature, pressure, rotation or time. Using multiplexing techniques, combinations of these sensing applications could be performed in a single compact device.

## Methods

**Sample preparation.** Sample preparation begins with a (100)-oriented, type IIa CVD diamond produced by chemical vapour deposition (Element 6) with dimensions of  $(3 \times 3 \times 0.3$  mm<sup>3</sup>). To increase NV ensemble density, the diamond was electron-irradiated at 4.5 MeV with a beam current of 20 mA over  $\sim 0.15$  m<sup>2</sup> and annealed for 2 h at 850 °C yielding  $\sim 0.1$  ppm NV centres. Characterized with absorption measurements ( $\alpha \approx 0.45$  cm<sup>-1</sup>), this concentration has adequate brightness to illuminate the pattern of the pump laser in the sample and allow for almost complete absorption of the pump while being low enough to preserve spin coherence properties. At low pump and microwave power levels, the ODMR linewidth is limited by the  $T_2^*$  coherence of the diamond, which is  $\sim 1$   $\mu$ s as characterized by free-induction decay measurements. All six surfaces of the diamond are polished to a mean surface roughness of  $\sim 2$  nm r.m.s. (characterized using atomic force microscopy, see Supplementary Information) with a 500  $\mu$ m input facet on one corner at 45° creating an entrance window for the laser (Fig. 1a). The diamond sample is thermally coupled to a brass sample holder with indium, which may cause additional absorption through evanescent coupling of the confined radiation. The thermal coupling also ensures that the device is in thermal equilibrium throughout the experiments, avoiding broadening in the ODMR linewidths. The sample holder is temperature-stabilized to  $21.6 \pm 0.1$  °C using a water chiller.

**Experimental set-up.** A spatially filtered, 532 nm single-mode longitudinal excitation beam from a Verdi V5 or a homebuilt 50 mW direct green laser diode (OSRAM) is focused into the input facet of the diamond sample. Both frequency and spatial multi-mode excitation is feasible as long as the beam shape can be focused to the size of the input facet, that is, below 300  $\mu$ m diameter. Three sets of perpendicular Helmholtz coils, with diameters ranging from 8 to 12 inches, provide a uniform static or slowly varying magnetic field. Noise floor measurements were taken with a Halbach ring to provide a static magnetic field. Using ODMR spectra recorded with the application of three different control fields, the rotation matrix from the Cartesian frame of the coils to the NV axis is determined. An impedance-matched loop antenna located  $\sim 5$  mm above the sample delivers microwave excitation, with 40 dBm on the transmission line. The microwave excitation is frequency modulated at 1.5 kHz with a modulation depth of 1 MHz. Fluorescence emission is collected with an aspheric condenser lens (NA = 0.79), followed by a 662–800 nm band-pass filter to minimize NV<sup>0</sup> contribution to the fluorescence. A second condenser lens images the fluorescence onto a balanced large-area photoreceiver (New Focus 2307), which minimizes the effect of low-frequency laser noise by balancing green input laser power. The system collection efficiency is  $\sim 17\%$  of the total fluorescence signal, which is demodulated using an SRS-850 lock-in amplifier.

Received 26 May 2014; accepted 24 February 2015;  
published online 6 April 2015; corrected online 3 September 2015

## References

- Balasubramanian, G. *et al.* Ultralong spin coherence time in isotopically engineered diamond. *Nature Mater.* **8**, 383–387 (2009).
- Stanwix, P. L. *et al.* Coherence of nitrogen-vacancy electronic spin ensembles in diamond. *Phys. Rev. B* **82**, 201201 (2010).
- Bar-Gill, N., Pham, L. M., Jarmola, A., Budker, D. & Walsworth, R. L. Solid-state electronic spin coherence time approaching one second. *Nature Commun.* **4**, 1743 (2013).
- Budker, D. & Romalis, M. Optical magnetometry. *Nature Phys.* **3**, 227–234 (2007).
- Taylor, J. M. *et al.* High-sensitivity diamond magnetometer with nanoscale resolution. *Nature Phys.* **4**, 810–816 (2008).
- Maze, J. R. *et al.* Nanoscale magnetic sensing with an individual electronic spin in diamond. *Nature* **455**, 644–647 (2008).
- Balasubramanian, G. *et al.* Nanoscale imaging magnetometry with diamond spins under ambient conditions. *Nature* **455**, 648–651 (2008).
- Fang, K. *et al.* High-sensitivity magnetometry based on quantum beats in diamond nitrogen-vacancy centers. *Phys. Rev. Lett.* **110**, 130802 (2013).
- Rondin, L. *et al.* Magnetometry with nitrogen-vacancy defects in diamond. *Rep. Prog. Phys.* **77**, 056503 (2014).
- Dolde, F. *et al.* Electric-field sensing using single diamond spins. *Nature Phys.* **7**, 459–463 (2011).
- Kucsko, G. *et al.* Nanometre-scale thermometry in a living cell. *Nature* **500**, 54–58 (2013).
- Toyli, D. M., Charles, F., Christle, D. J., Dobrovitski, V. V. & Awschalom, D. D. Fluorescence thermometry enhanced by the quantum coherence of single spins in diamond. *Proc. Natl Acad. Sci. USA* **110**, 8417–8421 (2013).
- Neumann, P. *et al.* High-precision nanoscale temperature sensing using single defects in diamond. *Nano Lett.* **13**, 2738–2742 (2013).



14. Wolf, T. *et al.* A subpicotesla diamond magnetometer. Preprint at <http://arxiv.org/abs/1411.6553> (2014).
15. Le Sage, D. *et al.* Efficient photon detection from color centers in a diamond optical waveguide. *Phys. Rev. B* **85**, 121202 (2012).
16. Jensen, K. *et al.* Cavity-enhanced room-temperature magnetometry using absorption by nitrogen-vacancy centers in diamond. *Phys. Rev. Lett.* **112**, 160802 (2014).
17. Ajoy, A. & Cappellaro, P. Stable three-axis nuclear-spin gyroscope in diamond. *Phys. Rev. A* **86**, 062104 (2012).
18. Hodges, J. S. *et al.* Timekeeping with electron spin states in diamond. *Phys. Rev. A* **87**, 032118 (2013).
19. Pham, L. M. *et al.* Magnetic field imaging with nitrogen-vacancy ensembles. *New J. Phys.* **13**, 045021 (2011).
20. Manson, N. B., Harrison, J. P. & Sellars, M. J. Nitrogen-vacancy center in diamond: Model of the electronic structure and associated dynamics. *Phys. Rev. B* **74**, 104303 (2006).
21. Lin, C.-K., Wang, Y.-H., Chang, H.-C., Hayashi, M. & Lin, S. H. One- and two-photon absorption properties of diamond nitrogen-vacancy defect centers: A theoretical study. *J. Chem. Phys.* **129**, 124714 (2008).
22. Wang, Z.-H. & Takahashi, S. Spin decoherence and electron spin bath noise of a nitrogen-vacancy center in diamond. *Phys. Rev. B* **87**, 115122 (2013).
23. Bar-Gill, N. *et al.* Suppression of spin-bath dynamics for improved coherence of multi-spin-qubit systems. *Nature Commun.* **3**, 858 (2012).
24. Acosta, V. M. *et al.* Temperature dependence of the nitrogen-vacancy magnetic resonance in diamond. *Phys. Rev. Lett.* **104**, 070801 (2010).
25. Fang, K. *et al.* High-sensitivity magnetometry based on quantum beats in diamond nitrogen-vacancy centers. *Phys. Rev. Lett.* **110**, 130802 (2013).
26. Narimanov, E., Fan, J. & Gmachl, C. in *Conference on Lasers and Electro-Optics/Quantum Electronics and Laser Science and Photonic Applications Systems Technologies* paper QWA7 (Optical Society of America, 2005); <http://go.nature.com/fvCZps>
27. Poem, E., Kaczmarek, K., Weinzetl, C., Nunn, J. & Walmsley, I. Broadband, noise-free optical quantum memory with neutral nitrogen-vacancy centers in diamond. Preprint at <http://arxiv.org/abs/1408.7045> (2015).
28. Matushita, S. & Campbell, W. H. (eds) *Physics of Geomagnetic Phenomena* (Academic Press, 1967).
29. Fagaly, R. L. Superconducting quantum interference device instruments and applications. *Rev. Sci. Instrum.* **77**, 101101 (2006).
30. Edelstein, A. Advances in magnetometry. *J. Phys. Condens. Matter* **19**, 165217 (2007).

### Acknowledgements

The authors would like to thank R.-J. Shiue, D. Rich, F. Dolde, G. Steinbrecher, T. Dordevic, E. H. Chen and O. Gaathon for helpful discussion. The authors would like to acknowledge D. Twitchen and M. Markham at Element Six Ltd for assistance with diamond irradiation. This work was supported by The Defense Advanced Research Projects Agency (government contract/grant number N66001-13-1-4027). The views, opinions, and/or findings contained in this article are those of the authors and should not be interpreted as representing the official views or policies, either expressed or implied, of the Defense Advanced Research Projects Agency or the Department of Defense. The Lincoln Laboratory portion of this work is sponsored by the Assistant Secretary of Defense for Research & Engineering under Air Force Contract number FA8721-05-C-0002 and the Office of Naval Research Section 321MS. Opinions, interpretations, conclusions and recommendations are those of the authors and are not necessarily endorsed by the United States Government. M.E.T. was supported by the NSF IGERT programme Interdisciplinary Quantum Information Science and Engineering (iQuiSE). T.S. was supported by the Alexander von Humboldt Foundation. H.C. is supported by the NASA Office of the Chief Technologist's Space Technology Research Fellowship.

### Author contributions

H.C., C.T. and D.B. performed the experiments. H.C., M.E.T., T.S., D.B. and D.E. conceived and designed the experiments. H.C. performed simulations. H.C., D.B. and D.E. prepared the manuscript. All authors reviewed the manuscript.

### Additional information

Supplementary information is available in the online version of the paper. Reprints and permissions information is available online at [www.nature.com/reprints](http://www.nature.com/reprints). Correspondence and requests for materials should be addressed to H.C., D.B. or D.E.

### Competing financial interests

The authors declare no competing financial interests.

# Corrigendum: Broadband magnetometry and temperature sensing with a light-trapping diamond waveguide

Hannah Clevenston, Matthew E. Trusheim, Carson Teale, Tim Schröder, Danielle Braje and Dirk Englund

*Nature Physics* **11**, 393–397 (2015); published online 6 April 2015; corrected after print 3 September 2015.

The version of this Letter originally published contained an error in the interpretation of the system noise floor resulting from lock-in amplifier filtering. Accordingly, Figs 4 and 5 (below) and the corresponding magnetic field sensitivity in the text have now been corrected in the online versions of the Letter.

**Figure 4**

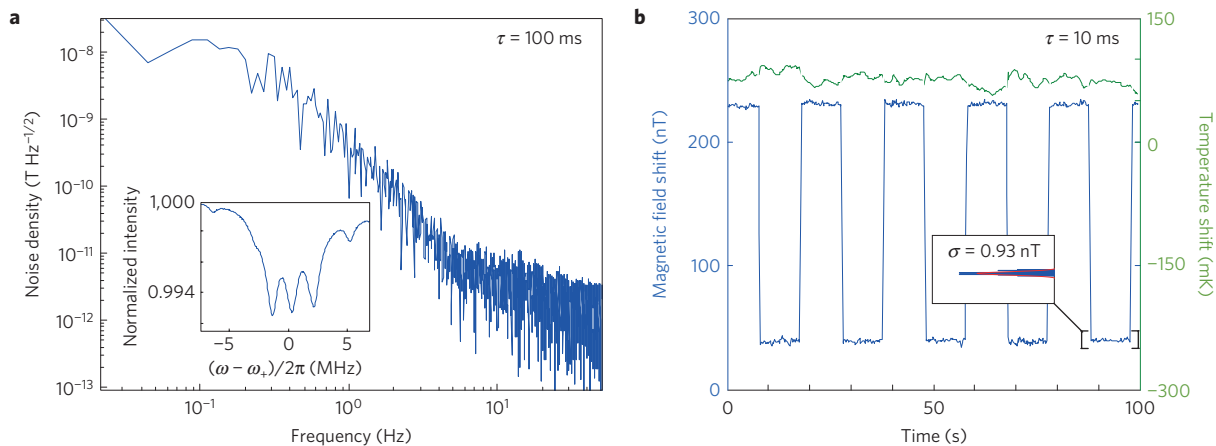


**Figure 5**

